



“The **more** opportunities there are to get **students involved**, the more you will **encourage** previously unreached and **unrepresented groups** to join the Earth and Space science community.”

Ryan Haupt
Research Fellow,
Smithsonian Museum
of Natural History
2015 Student Travel
Grant Recipient

Support the next generation of Earth and space scientists.
Donate to the Austin Student Travel Grant Challenge.

AGU100 ADVANCING
EARTH AND
SPACE SCIENCE

agu.org/austin | [#AGU100](https://twitter.com/AGU100)

Water Resources Research

RESEARCH ARTICLE

10.1029/2018WR023462

Key Points:

- Streamwise-oriented vegetation blades are modeled by patches of thin plates
- Large eddy simulations of flow through and around the patches allows examination of hydrodynamics and boundary layers
- Drag is quantified at element scale and at patch scale, and the influence of patch density is studied

Correspondence to:

T. Stoesser,
stoesser@cardiff.ac.uk;
t.stoesser@ucl.ac.uk

Citation:

Gong, Y., Stoesser, T., Mao, J., & McSherry, R. (2019). LES of flow through and around a finite patch of thin plates. *Water Resources Research*, 55. <https://doi.org/10.1029/2018WR023462>

Received 19 JUN 2018

Accepted 21 JUN 2019

Accepted article online 4 JUL 2019

LES of Flow Through and Around a Finite Patch of Thin Plates

Yiqing Gong^{1,2} , Thorsten Stoesser² , Jingqiao Mao¹ , and Richard McSherry²

¹College of Water Conservancy and Hydropower Engineering, Hohai University, Nanjing, China, ²School of Civil Engineering, Cardiff University, Cardiff, UK

Abstract Large eddy simulations (LESs) are performed for turbulent flow through and around a porous patch of thin vertical plates at a plate Reynolds number of $Re_p = 5,800$. The plates are arranged in a staggered pattern, presenting an elliptical planform and mimicking streamwise-oriented blades of emergent vegetation. The immersed boundary method is employed to explicitly resolve the interaction between flow and plates. Three flow cases, each with a different number of plates within the same planform area, that is, different patch density, are studied. The Reynolds number based on freestream velocity and plate length is the same in all cases. Inspection of the distribution of velocity and vorticity in the horizontal plane reveals that downstream plates are significantly impacted by the wakes from upstream plates. It is therefore proposed that the plates can be divided into two groups based on the local flow characteristics, which are a function of position within the patch: a free group and a wake group. This classification is subsequently used in the quantitative analysis of boundary layer development and drag force at plate scale. The thickness and character of the simulated boundary layers on the plates differ significantly from predictions based on analytical or empirical relationships, which is due to wake effects and the finite length of the plates. The simulations demonstrate the so-called sheltering effect; that is, the drag forces acting on downstream plates (in the wake group) are significantly lower than those acting on upstream plates, a result of the lower approach flow speed. Although the front-area-to-lateral-area ratio of the plates is low (1/40), pressure drag is observed to be larger than friction drag for each plate. The ratio of pressure drag to the total drag at patch scale shows only very little dependence on the plate density of the patch.

1. Introduction

Aquatic vegetation can improve water quality by modifying nutrient cycling and releasing oxygen through photosynthesis (Jones et al., 1994). The biological efficiency of vegetation in carrying out these processes is largely dictated by the local hydrodynamics, which is in turn dependent on the drag exerted by the plants. A sound understanding of these processes is therefore important for the design of river restoration and wetlands engineering (Stoesser et al., 2003).

Traditionally, many researchers have focused on vegetation resistance and various experiments have been carried out with natural and artificial plants (Kadlec, 1990; Kouwen et al., 1969). In flume experiments vegetation is generally idealized as a matrix of cylinders, which are considered to be good surrogates for plant stems or tree trunks (Nepf, 1999; Poggi et al., 2004). The flow around cylinders analogy is also widely adopted in numerical simulations of flow through vegetation since flow around an isolated cylinder has been thoroughly investigated and is well understood. The bulk drag coefficient, C_D , based on the cylinder Reynolds number, Re_D , can be directly used in drag force terms and drag-related turbulence terms in RANS models (Fischer-Antze et al., 2001; López & Garcia, 2001). However, for heterogeneous vegetation communities this simplification may lead to inaccuracies (Defina & Bixio, 2005), as interactions between plants may not be properly taken into account. Liu et al. (2008) demonstrated experimentally that the spatial heterogeneity of flow within a vegetation canopy is strongly dependent on plant density and Tanino and Nepf (2008) highlighted that the vegetation density is also a significant factor in determining the bulk drag coefficient. For stiff stems the pressure drag is dominant and can account for over 80% of the total drag (Vogel, 1994; Stoesser et al., 2010), and the cylinder-based model has contributed many valuable insights into such flows. It is not, however, well suited for the representation of vegetation foliage, which is shown to be a major contributor to the overall drag of a plant for many vegetation species such as leafy willows on the floodplains of

rivers and streams or instream vegetation such as eel grass. For these types of vegetation the flexible leaves or blades orient themselves with the flow to minimize their frontal area and thus minimize pressure drag. Hence, their flow resistance is believed to be mainly due to viscous skin friction drag (Miler et al., 2012). What follows is that instead of rigid cylinders, thin plates have been proposed as better geometric models to mimic blades/leaves of above mentioned aquatic vegetation (Wunder et al., 2018).

In addition to generating hydraulic drag, aquatic vegetation also fulfills an ecological role via mass exchange with the ambient flow. The mass transfer process is mainly dictated by the boundary layer in the immediate vicinity of blades (Nikora, 2010), and boundary layer concepts are widely utilized by ecologists in studying natural aquatic plants (Hurd et al., 1997; Statzner, 2008). Flow velocity increases from 0 at the blade surface to the bulk velocity of the incoming flow at the boundary layer edge, leading to a large velocity gradient and viscous effects play a role. The uptake rate of nutrients is found to be controlled by the thickness of the viscous layer, which is greatly dependent on the freestream flow conditions (Thomas et al., 2000). However, most studies on the hydraulics of vegetated flows consider larger-scale effects in channels and flumes whose beds are covered, either partially or completely, with plants. Detailed studies of the leaf-scale boundary layer are therefore scarce, especially under turbulent flow conditions. This is largely because accurate measurements at the blade scale are difficult to achieve in laboratory conditions. Eddy-resolving numerical techniques such as large eddy simulation (LES) or direct numerical simulation are capable of accurate predictions of turbulence across the most (or all) important energy-carrying scales, offer an opportunity to further the present understanding of flows through foliage at this detailed level. Stoesser et al. (2009) successfully modeled flow through vegetation stems idealized as cylinders with a no-slip boundary condition employed on the stem surface. Nezu and Sanjou (2008) and Okamoto and Nezu (2010) conducted LES of flow past arrays of thin plates that were oriented perpendicular to the bulk flow direction. Their results showed fairly good agreement with corresponding experimental data and confirmed the prediction that the vegetation-flow interaction can be accurately resolved using LES.

Vegetation communities grow not only in long, continuous meadows but also in patches of finite length and width on banks and floodplains. The discrete drag induced by these patches gives rise to significant spatial variation in the flow field. A number of recent studies have therefore focused on patch-scale hydrodynamics (Siniscalchi et al., 2012; Zong & Nepf, 2012). Circular patches of vegetation are often found after initial establishment of seedlings, and these have been widely studied both in the laboratory and in the field (Bouma et al., 2007; Follett & Nepf, 2012; Meire et al., 2014). The local erosion and deposition pattern are related to the vegetation growth, and the lateral extension of the patch is inhibited by erosion adjacent to the patch sides, where flow is locally accelerated (Bouma et al., 2009). In contrast, the wake zone provides more favorable conditions for plant growth, for example, due to increased nutrient deposition (Vandenbruwaene et al., 2011). As a result, the plants generally form approximately elliptical patches due to streamwise growth.

This study should be considered complementary to the experimental study carried out by Wunder et al. (2018) who carried out Particle Image Velocity measurements just upstream and downstream of an artificial vegetation patch (consisting of a collection of thin glass plates), which met the allometric characteristics of a real leafy plant. Their study revealed new information about the flow and turbulence structure downstream of the patch. In the study reported here, LES, a numerical method that allows the calculation of the most energetic part of a turbulent flow (Stoesser, 2014), is employed to simulate the instantaneous flow through a patch of thin glass plates arranged in a very similar geometrical configurations to the Wunder et al. (2018) study. The three principal objectives of the study are as follows: (1) to describe the detailed hydrodynamics of flow through idealized leaf/blade dominated vegetation, (2) to quantify and present plate-scale boundary layers and to evaluate their structure and quantities in comparison with empirical solutions for flat plate laminar boundary layers, and (3) to quantify the drag force at element scale and at patch scale for various patch geometries.

2. Numerical Framework

In this study, high-resolution LESs are carried out using the in-house code Hydro3D (Cevheri et al., 2016; Stoesser & Nikora, 2008). The code has been widely used and well validated in many different cases, including flow past and through various types of obstacles (Kara, Stoesser, McSherry, et al., 2015; Kim & Stoesser, 2011; Stoesser et al., 2010). The incompressible, turbulent, viscous flow is solved using the spatially filtered Navier-Stokes equations:

$$\nabla \cdot \mathbf{u} = 0 \quad (1)$$

$$\frac{\partial \mathbf{u}}{\partial t} + \mathbf{u} \cdot \nabla \mathbf{u} = -\nabla p + \frac{1}{Re_p} \nabla^2 \mathbf{u} - \nabla \cdot \boldsymbol{\tau} + \mathbf{f}, \quad (2)$$

where $\mathbf{u} = (u, v, w)^T$ is the filtered velocity vector and p is the filtered pressure divided by fluid density, Re_p is the Reynolds number based on the plate length, ($Re_p = L_p u_{\text{bulk}} / \nu$, where L_p is the length of the plate, u_{bulk} is the bulk velocity, and ν is the kinematic viscosity), $\boldsymbol{\tau}$ and $\mathbf{f} = (f_x, f_y, f_z)^T$ are source terms arising from the anisotropic part of the subgrid-scale (SGS) stresses and from the presence of the plates in the flow, respectively. Note that x , y , and z correspond to the streamwise, spanwise, and vertical directions, respectively.

The filtered equations are solved on a uniform Cartesian grid. The diffusive term is approximated by central differences of second-order accuracy, while the convective term is approximated with a fifth-order weighted essentially nonoscillatory scheme (Shu, 2009). The weighted essentially nonoscillatory scheme offers both sufficient computational accuracy and necessary algorithm stability to prevent the occurrence of numerical oscillations upstream of sharp solid bodies. The subgrid stresses are computed with the WALE model proposed by Nicoud and Ducros (1999) because it has proven great accuracy in previous LESs of flow past immersed bodies (Kara, Sturm, McSherry, et al., 2015; Kara, Sturm, McSherry, Mulahasan, et al., 2015; Ouro & Stoesser, 2017, 2018; Ouro et al., 2017). The force exerted from the no-slip boundary condition of a submerged body, such as the plates in this study, is accounted for by employing a direct forcing immersed boundary method (IBM; Kara, Stoesser, McSherry, et al., 2015). This method enables the communication of velocities and forces between the solid boundary and ambient fluid via delta functions, which are refined with the kernel ϕ^* (Roma et al., 1999). The force term calculation is inserted into a three-step Runge-Kutta predictor to integrate the equations in time and a Poisson pressure-correction equation is used for coupling the pressure to the flow field in the final step. The code employs a hybrid MPI/OpenMP parallelization strategy (Ouro et al., 2019) and is executed on a high-performance computer.

3. Setup and Boundary Conditions

The LESs are designed to complement a series of laboratory experiments conducted at the University of Hull (Wunder et al., 2018). A fully developed channel flow approaches a porous artificial vegetation patch consisting of thin plates of length L_p arranged in a staggered pattern (Figure 1). The Reynolds number of this flow is $Re_p = 5,800$ and considers the bulk (or mean approach flow) velocity and the length of an individual plate. The computational domain spans $19.2L_p \times 9.6L_p \times 2.4L_p$ in the streamwise, spanwise, and vertical directions, respectively. The extent of the domain is selected as a compromise between the necessity for a domain that is large enough to cover all relevant turbulent flow structures, the requirement for very high grid resolution in critical areas and the desire to keep computation costs to a reasonable level. The domain is discretized with a uniform grid of $768 \times 384 \times 96$ points (≈ 28.3 million in total). The grid cell size in the y direction is half that of the x and z directions ($2\Delta y = \Delta x = \Delta z = 0.025L_p$) to provide greater resolution in the direction of the plate boundary layers.

Figure 2 shows a close-up of the grid in the x - y plane in the vicinity of two plates. The upper plate in this figure depicts the exact plate geometry featuring a plate-width-to-plate-length ratio of $B_p/L_p = 1/40$. This ratio is considered to be representative of ratios observed in natural vegetation leaves/blades. The lower plate in this figure is represented as a set of regularly spaced Lagrangian markers, which are spaced in accordance with the grid, and these points are used by the immersed boundary solver to compute the interaction force between the solid body (plate) and the Eulerian fluid. The IBM ensures the no-slip condition of the plate surface, and it permits the calculation of the total drag force exerted on each plate by summing up the forces of the individual immersed boundary points. A validation of the accuracy of this treatment is given in the next section.

The porous patch, centrally located in the computational domain, comprises five columns of plates and the patch occupies an approximately elliptical area in the horizontal plane, similar to the configuration of natural aquatic macrophytes (Figure 1). Three cases with varying vegetation density, ϕ , are considered in this study. The vegetation density of an elliptical patch is defined as follows:

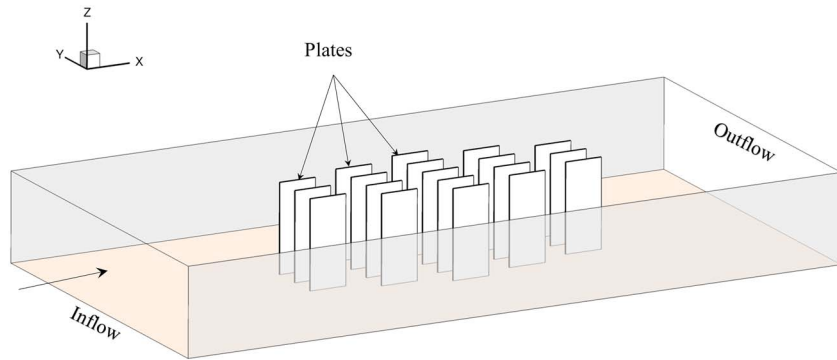


Figure 1. Computational domain.

$$\phi = \frac{n_p L_p B_p}{\pi ab}, \quad (3)$$

where n_p is the total number of plates per patch, a is the semimajor axis, and b is the semiminor axis. Increasing vegetation density is achieved by increasing the total number of plates, n_p , within the same patch area, as depicted in Figure 3. The streamwise spacing between neighboring columns of plates, s , is constant across all cases, whereas the spanwise spacing, s_i ($i = 1, 2, 3$), is varied. In all cases the major axis of the elliptical patch, $A = 2a$, is $10.6 L_p$ and the minor axis, $B = 2b$, is $3.6 L_p$. The salient parameters for these three cases are provided in Table 1.

In all cases the plant density is relatively low, due to the extremely thin plates used. Although the contribution of bed friction to the total drag force is always assumed to be negligibly small in vegetated flows, Kim and Stoesser (2011) found that this assumption may be invalid at low vegetation density. In order to eliminate the interference from bed and side wall shear stresses, periodic boundary conditions are employed in the spanwise and vertical directions. Hence, the total energy loss is exclusively due to the drag of the plates and the mean flow can be considered uniform in the vertical direction. In addition, the synthetic eddy method (SEM) proposed by Jarrin et al. (2006) is employed at the inlet boundary to generate fully developed turbulence in the form of prevailing coherent structures. The SEM reproduces prescribed first- and second-order statistics as well as characteristic length and time scales (Jarrin et al., 2006). Jarrin et al. (2006) have demonstrated its ability to produce realistic inflow conditions for a fully developed turbulent channel flow. At the outlet a convective boundary condition is applied, which ensures that coherent structures leave the compu-

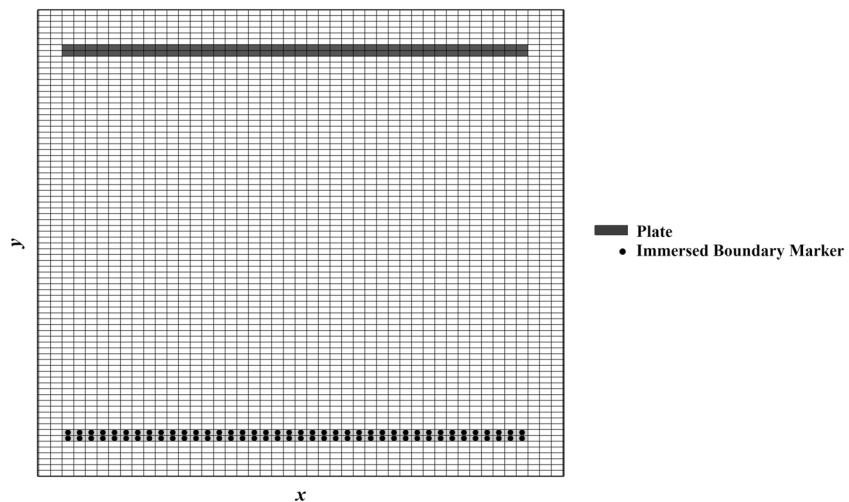


Figure 2. Section of the computational grid showing two thin plates. The upper plate shows the exact plate geometry, whereas the lower plate shows the immersed boundary points employed to enforce the no-slip condition. The immersed boundary method is used for all plates.

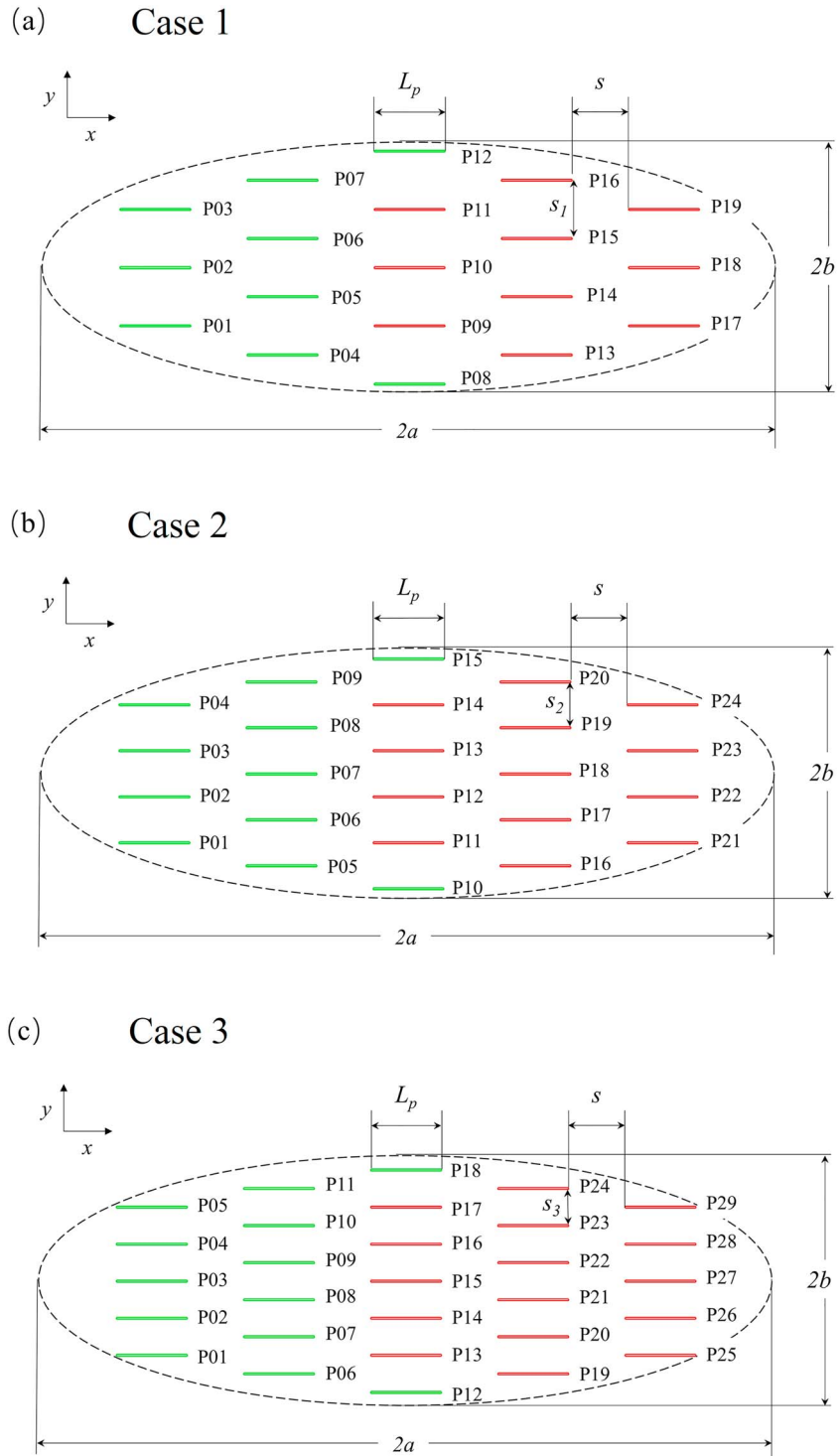


Figure 3. Patch configurations: (a) Case 1, (b) Case 2, (c) Case 3.

tational domain without causing numerical instabilities near the outlet. The intensity of the synthetically generated turbulence is set to 0.05, which is considered to be broadly representative of turbulence in natural open channel flows. These conditions are applied for all three LES presented in this paper. The simulations are initially run for approximately 20 patch flow through times, $T(= A/u_{\text{bulk}})$, to allow the flow to fully develop and are then continued for another $50T$ to acquire turbulence statistics.

Table 1
Key Geometric and Hydraulic Parameters

Case	n_p	ϕ	s/L_p	s_i/L_p	Re_p
1	19	0.0158	0.800	0.800	5,800
2	24	0.0200	0.800	0.625	5,800
3	29	0.0242	0.800	0.500	5,800

4. Validity and Credibility of the LES

In order to assess the validity and hence the credibility of the results of the patch flow simulations, two preliminary LES are carried out for a flow that resembles the patch flow and for which an analytical solution exists, which is Poiseuille flow, that is, a fully developed flow between two plates. The simulations use exactly the same grid as the patch flow simulations and while the first simulation uses a no-slip boundary condition, the second simulation treats the wall boundary with the IBM, that is, analogue to the main simulation (Case 1). In order to achieve Poiseuille flow, a periodic boundary condition is used in the streamwise direction (instead of a freestream inflow) to allow for the boundary layer to become fully developed. In a Poiseuille flow the velocity profile can be calculated as follows:

$$u(y) = -\frac{1}{2\mu} \frac{dp}{dx} y(H - y), \quad (4)$$

where dp/dx is the pressure gradient required to maintain the bulk velocity u_{bulk} which is equal to the freestream velocity of the patch flow simulations. H is the distance-between-plates, and here H equals s_1 . The maximum velocity in a Poiseuille flow is calculated as follows:

$$u_{\text{max}} = -\frac{H^2}{8\mu} \frac{dp}{dx} \quad (5)$$

or from:

$$u_{\text{max}} = \frac{3}{2} \bar{u} = \frac{3}{2} u_{\text{bulk}}. \quad (6)$$

With the goal to mimic Case 1, a Reynolds number of $Re = 4,640$ and a bulk velocity of $u_{\text{bulk}} = 1.0$ are prescribed from which $u_{\text{max}} = 1.5$ and $dp/dx = -0.00259$ can be calculated. The validation simulation yields $u_{\text{max}} = 1.5019$ and $dp/dx = -0.00260$ for the IBM simulation and hence an error in predicting these integral quantities of significantly less than 1%. The predicted velocity profiles of the two preliminary simulations and the analytical profile are presented in Figure 4. As can be seen the LES data points collapse entirely onto the analytical profile irrespective of wall treatment suggesting that the current grid and the use of the IBM are adequate and accurate.

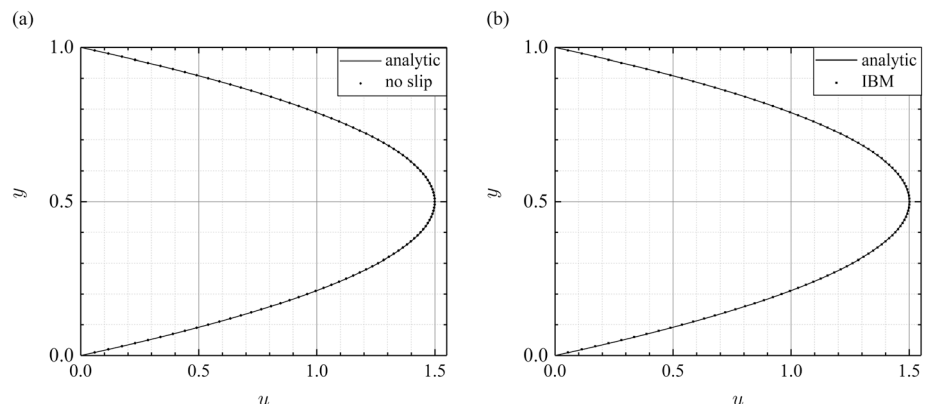


Figure 4. Computed and analytical velocity profiles for a Poiseuille flow when using (a) the no-slip wall boundary condition and (b) the immersed boundary method (IBM).

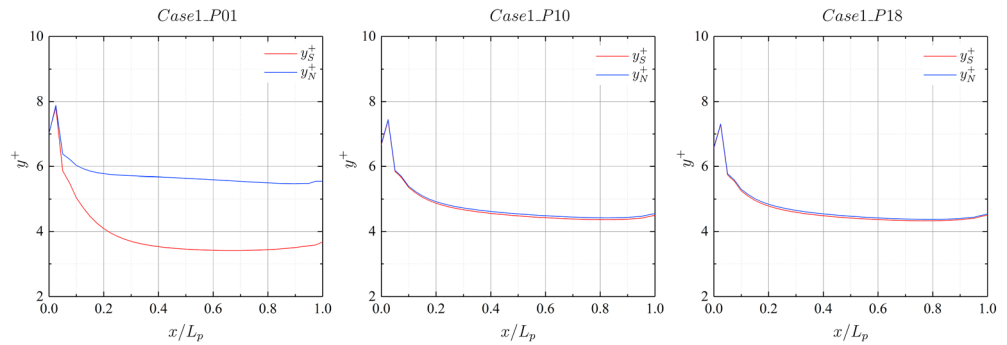


Figure 5. Distribution of the vertical grid spacing in wall units at the first grid point off the plates for P_{01} , P_{10} , and P_{18} of Case 1.

Further assessment of the validity/credibility of the results when using the immersed boundary wall treatment method is by ensuring that the first grid point off the plate is located in the viscous sublayer. In Figure 5 the dimensionless grid spacing y^+ at the first grid point off the plate is plotted as a function of (dimensionless) distance from the leading edge of the plate, x/L_p for plates P_{01} , P_{10} , and P_{18} . The dimensionless wall distance peaks immediately after the leading edge, which is owing to the fact that the plate is not infinitely thin but causes a stagnation point and thus some acceleration past the leading edge of the plate. A maximum of $y^+ \approx 8$ is observed near $x/L_p = 0.0$, however, most of the y^+ values are below 5 and hence well within the viscous sublayer. For plate P_{01} , where the flow over the plate is expected to be different on the upper (north) and lower (south) side of the plate, the y^+ values on the south side of the plate (red line) are lower than the y^+ values on the north side (blue line). The flow over the lower (or south) side of the plate resembles a classical boundary layer flow (with a quasi-undisturbed freestream away from the plate), whereas the flow over the upper (north) side of the flow resembles a developing Poiseuille flow. The plots demonstrate, again, that the chosen grid spacing in the wall-normal direction is adequate.

Finally, the potential influence of the subgrid-scale model on the accuracy of the simulation is investigated by plotting the ratio of the subgrid-scale (kinematic) viscosity to the molecular (kinematic) viscosity, ν_{sgs} / ν . Figure 6 presents contours of ν_{sgs} / ν at an instant in time and inside the patch of Case 1. The subgrid-scale viscosity ν_{sgs} is of the same order as the molecular viscosity and in fact its maximum attains only approximately 2.8 times the molecular viscosity inside the eddies, a clear indicator that the influence of the sgs-viscosity on the flow is deemed negligible. Also noteworthy is that ν_{sgs} is near zero in the vicinity of the plates except very close to the leading edge.

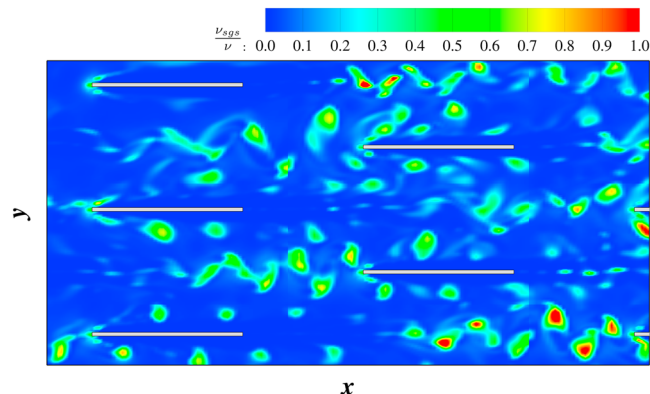


Figure 6. Contours of the instantaneous subgrid-scale-viscosity normalized by the molecular viscosity, ν_{sgs}/ν , in the vicinity of a plate.

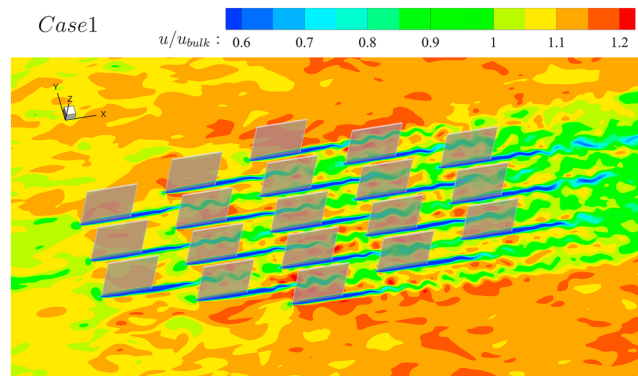


Figure 7. Instantaneous streamwise velocity in the near-patch region at half depth: Case 1.

5. Results and Discussion

5.1. Patchflow Hydrodynamics

Figure 7 presents contours of the instantaneous streamwise velocity, normalized by the bulk velocity, in the horizontal plane at half depth ($z = 1.2L_p$) for Case 1. The existence of the porous patch significantly influences the global flow structure. Inside the patch, flow is decelerated due to blockage effects, whereas on the either side of it flow is locally accelerated to satisfy global mass conservation. The flow field can then be divided into two regions based on the flow rate—inside the patch and outside it. Nonetheless, due to the relatively low blockage, the flow velocity is generally in the range $0.8 < u/u_{\text{bulk}} < 1.2$ throughout most of the domain, with only very thin regions of localized low speed flow in the wakes of the individual plates. The figure shows that the thin plates shed continuous streets of vortices into their wakes, which is common for bluff bodies whose width-to-length ratios are approximate to or greater than 1.0 (Nepf, 2011). Similar flow patterns, including vortex wakes, have been observed in laboratory and field measurements of flows through circular and rectangular patches (Bouma et al., 2007; Chen et al., 2012).

To better visualize the vortex shedding behind the plates the distribution of vertical vorticity, ω_z , in the x - y plane at half depth is shown in Figure 8. The regions of approximately constant high vorticity adjacent to the plates' surface are the result of high shear within the boundary layer, while the discontinuous regions behind the plates are the result of fluid rotation in the form of trailing edge vortices. The vortical structures are greatly affected by the plate location within the patch. The flow structure around certain plates appears to be relatively unaffected by the presence of other plates in the patch, whereas for others the flow is significantly affected by other plates. Plate P_{08} (see Figure 3a) is an example of a plate whose flow is largely independent of other plates: Regular vortex pairs are propagated and gradually dissipated in its wake in manner similar to that of a classic von Karman vortex street. Other plates, however, are significantly affected by vortex wakes from upstream plates and any vorticity generated at their surfaces is superimposed onto existing vortices that have been generated by upstream plates. As a result, the vertical vorticity distribution in the wake zone of the patch itself is quite chaotic owing to the eddy superposition occurring within it. Based on this analysis

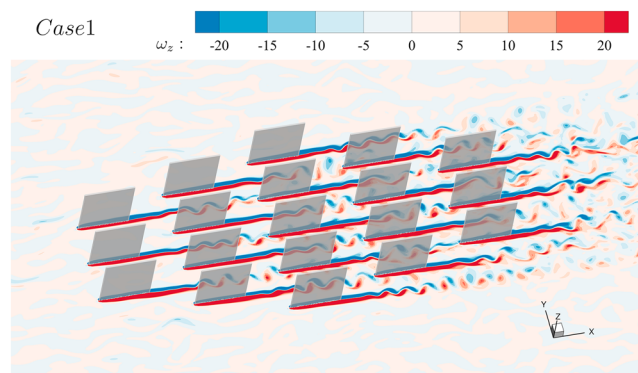


Figure 8. Instantaneous vertical vorticity in the near-patch region at half depth: Case 1.

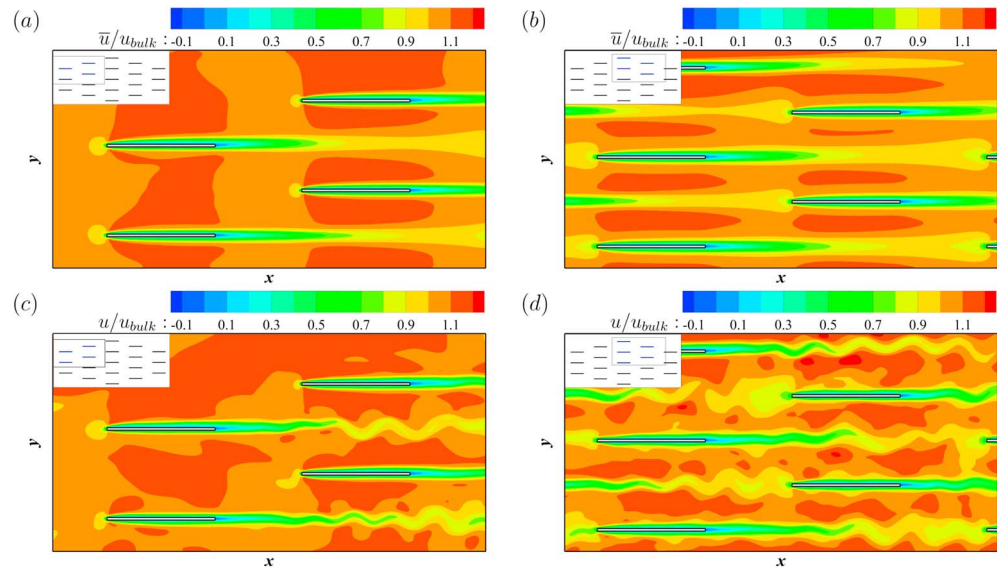


Figure 9. Contours of normalized time-averaged streamwise velocity (a, b) and normalized instantaneous streamwise velocity (c, d) for the free group and the wake group (their position within the patch is indicated in the sketch in the upper left corner).

it is proposed that the patch can be divided into two groups of plates, depending on their relative positions. The plates of the “free group,” that is, drawn in green in Figure 3, are plates that are unaffected by the wakes of upstream plates, whereas the plates of the “wake group,” drawn in red in Figure 3, are plates that are located in the turbulent wakes of at least one upstream plate.

Figure 9 compares the local streamwise velocity fields at half depth for the two plate groups. Figures 9a and 9b present the time-averaged velocity, while Figures 9c and 9d present the instantaneous streamwise velocity. In both groups it can be seen that the flow adjacent to the plates’ surface is decelerated by virtue of viscous drag, leading to the formation of a thin boundary layer above (and below) the plates. The resulting spanwise mass flux causes localized regions of high streamwise velocity outside of the boundary layers in both groups. This may be considered a developing Poiseuille flow, and it takes place in the gap between two neighboring plates of the free group (Figure 9a). Although the plates have a very low width-to-length ratio (1/40), the approach flow is nonetheless noticeably decelerated upstream of the leading edges of the plate. These low-velocity regions upstream of the plates of the second row are smaller than those of the first row because the oncoming flow has been accelerated between the upstream plates. For the wake group (Figure 9b) the low-velocity regions are engulfed within the wakes of the upstream plates. The downstream plates encounter slower oncoming flow and thus have thicker boundary layers due to lower local shear. In the free group, turbulent oscillations are damped out to maintain a viscous boundary layer on the plate surfaces. For plates in this group the spanwise gradient of instantaneous streamwise velocity is approximately constant along the length of the plate (Figure 9c), and as a result the instantaneous flow field in this region is very similar to the time-averaged field. In the wake group shown in Figure 9d, vortices generated by upstream plates transfer kinetic energy toward the plate surfaces, causing turbulent fluctuations in this region. Viscous damping in the boundary layer is not sufficient to suppress these fluctuations entirely, and thus, the surface of the boundary layer is disturbed by the enhanced turbulence. As a result, the outer part of the boundary layer is characterised by turbulent fluctuations along the length of the plate whereas the inner part remains streamlined. The boundary layer of the wake group is consequently divided into a steady viscous sublayer and an unsteady buffer layer.

5.2. Plate Boundary Layer

As described above, a boundary layer forms starting at the leading edge of each plate and grows until its trailing edge. The thickness of this layer is an important indicator of the local flow properties. Although local fluid velocities are observed to exceed u_{bulk} in this study, the edge of the boundary layer is nonetheless defined in the classical way as the distance from the plate surface at which $\bar{u} = 0.99u_{\text{bulk}}$. For a laminar boundary layer with uniform upstream flow, the boundary layer thickness (δ_{99}) can be calculated based on

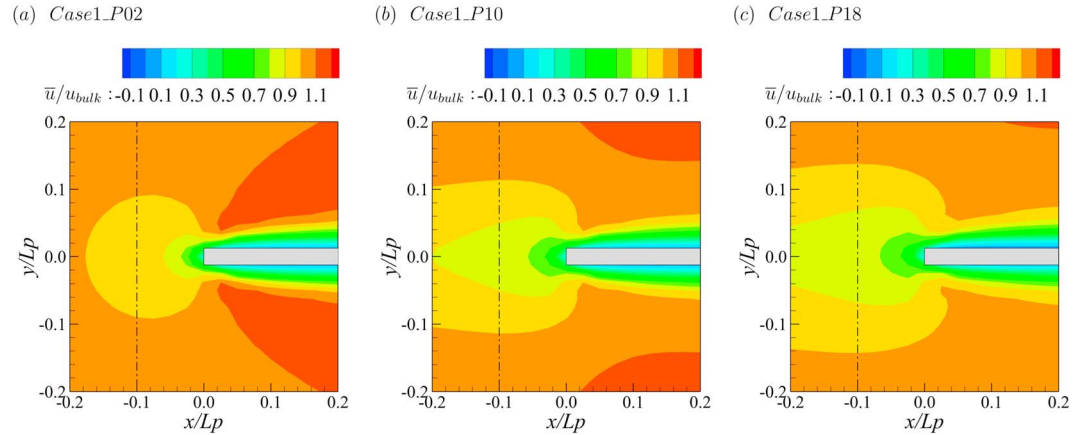


Figure 10. Contours of the time-averaged streamwise velocity around the leading edges of the (a–c) three plates along the centerline in Case 1. The dash-dotted line denotes the line along which velocity profiles have been extracted.

the Blasius solution as follows:

$$\delta_{99} = 5.0 \sqrt{\frac{\nu x}{u_{\text{bulk}}}} = 5.0 Re_x^{-1/2} x, \quad (7)$$

where $Re_x = u_{\text{bulk}} x / \nu$ is the Reynolds number using the streamwise distance, x , from the leading edge. The thickness $\delta_{99}(x)$ increases with increasing x until reaching laminar/turbulent transition which is when perturbations overcome viscous damping, typically occurring around $Re_x = 5 \times 10^5$. In the present study the maximum Reynolds number based on the plate's length is significantly lower than this critical value ($Re_p = 5.8 \times 10^3$) and laminar boundary layers would therefore be expected. However, quantitative analyses of the boundary layers suggest that this is not necessarily the case, as will be discussed below.

5.2.1. The Effect of Streamwise Velocity on the Plate Boundary Layer

In the Blasius boundary layer solution, the plate thickness is assumed to be infinitesimally small. Thus, the plate has no effect on the approach flow; that is, the freestream velocity profile is uniform with $\bar{u} = u_{\text{bulk}}$ at the leading edge. Also, the flow rate outside the boundary layer is also assumed to be uniform with $\bar{u} = u_{\text{bulk}}$. Although in this study the width-to-length ratio of the plates is very small ($1/40$), the oncoming flow nonetheless undergoes noticeable deceleration immediately upstream of the plates and is accelerated around the sharp leading edges of the plates. Figure 10 depicts contours of normalized streamwise velocity around the leading edges of the three plates that are positioned along the patch's centerline in Case 1. The three flow fields are symmetric about the centerline; that is, $y/L_p = 0.0$. The low-velocity region upstream of the plate's leading edges is shown to increase in size with each successive plate, which is the result of the progressively increasing wake of upstream plates. The downstream plates experience a visible increase in boundary layer thickness. A more quantitative picture of this behavior is provided with the help of Figure 11. Figure 11a presents velocity profiles at $x = -0.1L_p$, that is, slightly upstream of the plate leading edge (see dashed line in Figure 10), where $y/L_p = 0$ denotes the plate's center. The plot confirms that, in contrast to the uniform freestream upstream of the plate that is assumed in the Blasius solution, the approach flow velocity is markedly lower in the vicinity of the plate. The oncoming flow velocity upstream of the plates of the free group (here exemplary P_{02}) is approximately 96% of u_{bulk} and significantly higher than the approach flow velocity experienced by the plates of the wake group (here P_{10} and P_{18}), which drops to approximately 85% of the bulk velocity.

Figure 11b presents the computed distribution of the boundary layer thickness (δ_{99_LES}) as a function of distance from the plate's leading edge for the three plates, which are located along the patch centerline for Case 1. Also plotted is the Blasius solution and an envelope (shaded area) of various approximations of δ_{99} as derived from parabolic, cubic, and sine wave velocity profile equations (as given in Munson et al., 2012). For a laminar boundary layer, where viscous effects are dominant, the thickness is negatively proportional to the square root of velocity, namely, $\delta_{99_LES} \propto \sqrt{1/u}$ based on theoretical analysis. The boundary layer profile above P_{02} is mainly within the range of these analytical solutions because it can be assumed to be entirely laminar and the approach flow upstream of the plate is reasonably uniform. However, the velocity of the oncoming flow of P_{02} is less than the bulk velocity ($u < u_{\text{bulk}}$) in the vicinity of the plate but slightly

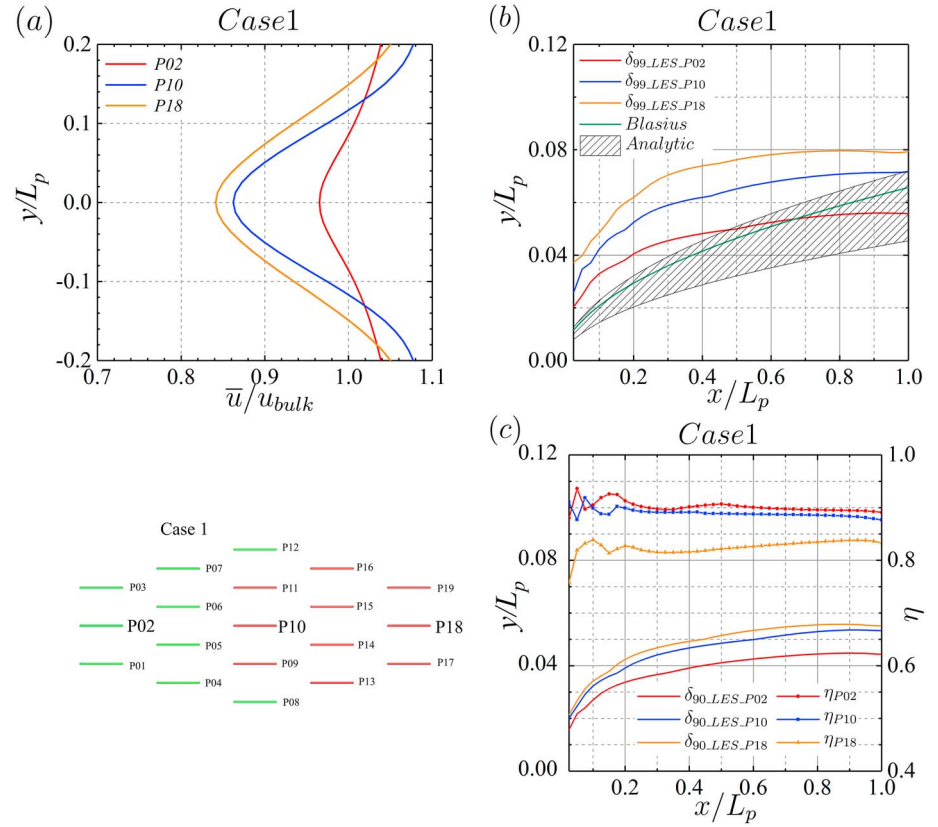


Figure 11. (a) Streamwise velocity profiles just upstream of the plates located along the centerline (P02, P10, and P18) of the patch of Case 1; (b) computed boundary layers together with the Blasius solution (green line) and an envelope of empirical boundary layer solutions (hashed area) for centerline plates P02, P10, and P18 of Case 1, and (c) viscous sublayer thickness (solid lines) and corresponding ratio of viscous-layer-thickness-to-boundary-layer-thickness (solid lines with markers) for centerline plates P02, P10, and P18 of Case 1.

greater the bulk velocity ($u > u_{bulk}$) away from the plate, and hence, the boundary layer thickness is therefore slightly overestimated near the front of the plate ($x/L_p < 0.6$) in comparison to the Blasius solution. In contrast, the underestimation of the boundary layer thickness over the rest of the plate can be explained by the accelerating (Poiseuille) flow between two plates. The boundary layer above P_{02} penetrates into the shaded area but exhibits a slower growth of the boundary layer in the second half of the plate and even asymptotic behavior suggesting that the profile is almost fully developed by the trailing edge of the plate.

For the other two plates on the patch centerline, which are considered members of the wake group, the boundary layer is much thicker and appears to comprise the viscous sublayer and buffer layer as described by turbulent boundary layer theory. The boundary layers on these plates are not entirely laminar anymore (the profiles are significantly above the Blasius solution) due to oncoming turbulence, which is a result of trailing edge vortex shedding from upstream plates. For these plates the location where the time-averaged velocity reaches 90% of u_{bulk} is used to define the viscous sublayer thickness; that is, $\delta_{90_LES} = \delta_{vis}$. For the viscous sublayers, the inversely proportional relationship remains valid in linking their thickness to the oncoming flow velocity and this is illustrated in Figure 11c. The relative increase in boundary layer thickness from P_{02} to P_{10} is dramatic (i.e., free-group- vs. wake-group-boundary-layers), while boundary layers of P_{10} and P_{18} are quite similar in magnitude and shape (both considered wake-group-boundary-layers).

A ratio index (η) is introduced to evaluate the turbulence intensity in the buffer layer as follows:

$$\eta = \sqrt{\frac{\delta_{vis}}{\delta}} = \sqrt{\frac{\delta_{90_LES}}{\delta_{99_LES}}}. \quad (8)$$

For laminar/viscous boundary layers where the velocity profile can be assumed to be parabolic, the value of η should equal 90%/99% ≈ 0.90 . If the buffer layer is thickened because of enhanced turbulence, it is

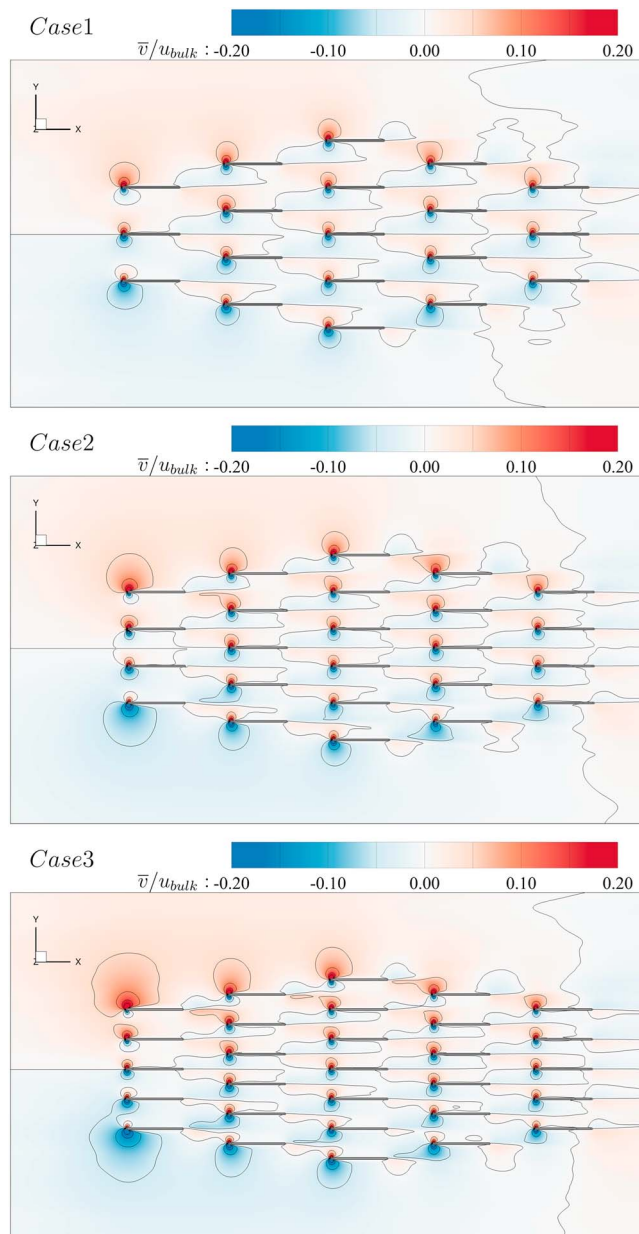


Figure 12. Contours of the normalized time-averaged spanwise velocity in the horizontal plane at half water depth.

hypothesized that η will decrease due to the relatively thin viscous sublayer. Figure 11c plots η for the three plates on the right y axis. The ratio for P_{02} is around 0.9, indicating a laminar boundary layer, and drops a little for P_{10} with the occurrence of the buffer layer but decreases significantly for P_{18} due to the more severe turbulence in the buffer layer.

5.2.2. The Effect of Spanwise Fluxes on the Plate Boundary Layer

In general, the spanwise momentum equation is omitted from boundary layer theories such as the Blasius solution or Poiseuille flow, respectively. The assumptions $v = 0$ or $dv/dy = 0$ are considered reasonable for flow over a plate of infinitesimal thickness (Blasius) or for a fully developed boundary layer in a straight pipe of infinite length (Poiseuille). However, for the present case of a porous patch consisting of staggered thin plates, spanwise velocities at various points in the domain are large enough to result in spanwise fluxes. Figure 12 presents contours of the normalized time-averaged spanwise velocity in the horizontal plane at half water depth for the three cases. Upstream of the patch the fluid diverges from the centerline due to the flow blockage that the patch presents. Each plate within the patch splits the oncoming flow at its leading edge,

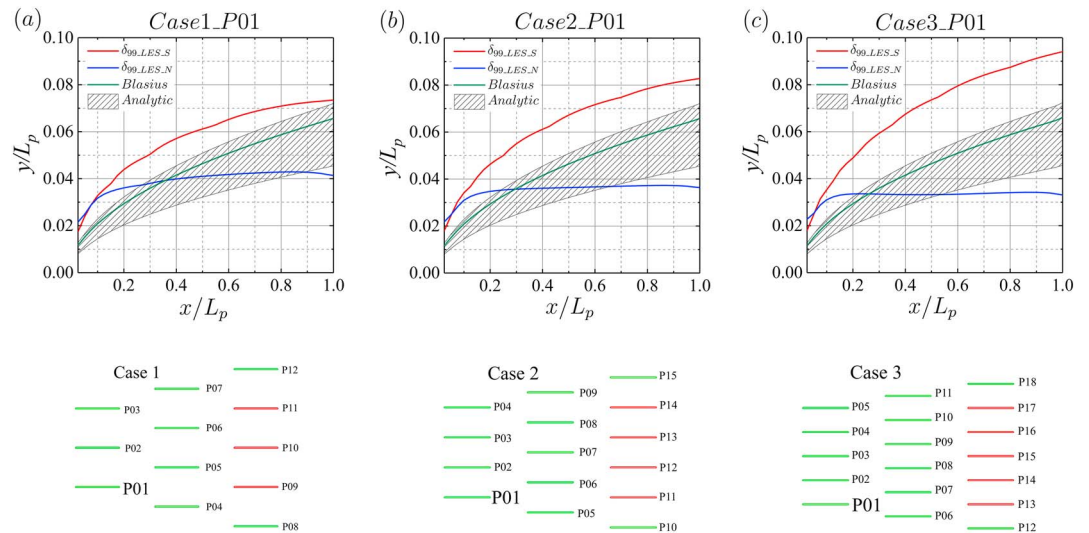


Figure 13. Boundary layers of the plates situated at the leading edge of the patch. (a) Upper (blue) and lower (red) boundary layer thickness of plate P_{01} of Case 1. (b) Upper (blue) and lower (red) boundary layer thickness of plate P_{01} of Case 2. (c) Upper (blue) and lower (red) boundary layer thickness of plate P_{01} of Case 3.

creating distinct velocity gradients. Dependent on the individual plate location, the flow around the plate can be symmetric or asymmetric. This is most obvious when comparing the spanwise velocity distribution around a plate that is located on the centerline with the one of a plate that is located at the periphery of the patch. Regions of nonzero spanwise velocity at the leading edges of the outermost plates are visible, and it is evident that magnitude and extent of these regions increase with increasing patch density. It can therefore be concluded that the amount of fluid diverted to the sides of the patch increases with increasing patch density.

Fully developed flow between two parallel plates is considered Poiseuille flow, and in this study the flow between two opposite plates is developing from the leading edge, where the boundary layer above one plate grows in the spanwise direction until it meets the boundary layer of the opposite plate. In Poiseuille flow the length of the developing region is typically around ten times the plate-to-plate distance (normal to the flow), which is much longer than the plate length in the present study, that is, with a maximum plate-length-to-plate-distance ratio of 2 for Case 3 (see Table 1).

Figure 13 presents boundary layers developing along either side of plate P_{01} of the three cases. P_{01} is a free-group plate, which is located at the leading edge of the corresponding patch. The blue boundary layer is the one that develops in the gap between P_{01} and P_{02} , whereas the red boundary layer is the one that develops pretty much undisturbed. Noteworthy is the fact that the developing Poiseuille flow boundary layer thickness is less in the denser patch. Also, the deviation from Blasius-type boundary layer is very obvious due to the asymptotic behavior of the Poiseuille flow. As can be appreciated from Figure 12 the denser the patch, the more significant the spanwise fluxes around P_{01} , and hence, the (red) free-flow boundary layers of P_{01} of Cases 1, 2, and 3 grow much more significant than the boundary layer of the Blasius solution (assuming the absence of spanwise fluxes). Whereas the boundary layer thickness below P_{01} of Case 1 is approximately 10% greater than the Blasius-type boundary layer thickness, it is approximately 50% greater than the Blasius boundary layer thickness below P_{01} of Case 3. The flow around individual plates, that is, the plate scale, is clearly affected by the hydrodynamics at patch scale.

5.2.3. The Effect of Patch Density on the Plate Boundary Layer

Flow passes through the patch rather than just diverting and moving around it as would be the case for flow past a solid body. The density of the porous patch determines the ratio of through flow to diverted flow (Rominger & Nepf, 2011). In the present LES cases, the patch density is increased by reducing the spanwise spacing of the plates, s_i , with the goal to have more plates in the same area. The added plates alter the flow field, noticeable the spanwise velocity distribution as shown in Figure 12.

In order to evaluate the impact of increased patch density on the boundary layer characteristics, the approach flow profile and the boundary layer thickness above the three centerline plates of Case 1 (P_{02} , P_{10} , and P_{18}) and Case 3 (P_{03} , P_{15} , and P_{27}) are presented in Figure 14.

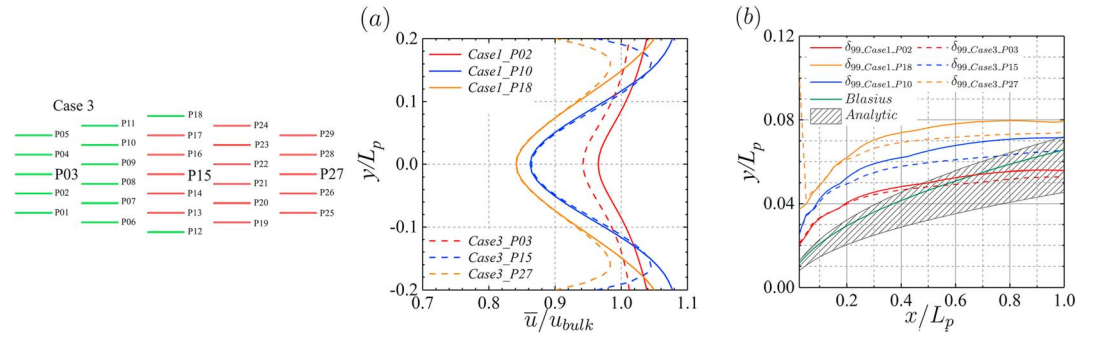


Figure 14. Definition sketch of the patch of Case 3 and (a) approach flow velocity profiles upstream of the three centerline plates for Case 1 (solid lines) and Case 3 (dashed lines) and (b) boundary layer thickness above the three centerline plates.

The plate density affects the velocity profile upstream of the patch. The (minimum) velocity upstream of P_{02} (free-group centerline plate of Case 1) is approximately 4% higher than the velocity upstream of P_{03} , that is, the free-group centerline plate of Case 3. This is due to the increased flow diversion in Case 3, the result of the increased patch density. Quite remarkably, the upstream velocities of the wake-group plates are nearly identical and hence are not affected by the patch density. On the other hand, the boundary layer characteristics differ regardless of whether the plates belong to the free-group or to the wake group. The boundary layers above the centerline plates of Case 3 develop in a manner that is qualitatively very similar to those of Case 1; that is, the further the plates are away from the leading edge of the patch, the thicker the boundary layer is, which is the result of the increased turbulence in the approach flow. However, although the plates are located at the same relative positions within the patch, the boundary layers of Case 3 are noticeably thinner than those of Case 1, and this is due to the closer proximity of the neighboring plate. In analogy to Poiseuille flow, the distance to the upper plate limits the growth of the boundary layer to half channel width and even though the plates are not long enough for the flow to fully develop. There is nevertheless a similar asymptotic behavior of the boundary layer regardless of patch density and relative plate position.

5.3. Drag Force and Drag Coefficients

Experimental measurement of the drag force exerted on individual vegetation elements in a flow requires the use of force sensors or other devices (Albayrak et al., 2012), while in the LES method employed in the present study it can be obtained directly by summing up the forces exerted by the individual immersed boundary points that collectively make up the plate geometry. The overall drag for the i th plate, F_i , is the sum of the viscous drag acting on the plate sides and the form drag due to the frontal area:

$$F_i = F_f + F_p \quad (9)$$

$$F_f = \frac{1}{2} C_{Df} A_s u_{bulk}^2 \quad (10)$$

$$F_p = \frac{1}{2} C_{Dp} A_f u_{bulk}^2, \quad (11)$$

where F_f is the friction drag, C_{Df} the friction drag coefficient, $A_s = L_p H_p$ is the plate's lateral area, F_p is the pressure drag, C_{Dp} the pressure drag coefficient, and $A_f = B_p H_p$ is the plates' frontal area. The bulk approach flow velocity is used irrespective of the plates position for consistency and to allow direct comparison of the so obtained forces. The friction drag F_f can be computed by integrating the shear stress within the boundary layers over the plate's lateral area, while the corresponding value of C_{Df} based on the Blasius solution is given by

$$C_{Df} = \frac{1.328}{\sqrt{Re_p}} = 0.0174. \quad (12)$$

Table 2
Drag Characteristics at Plate and Patch Scale for Case 1

Plate	F_i/F_t (%)	F_i/F_a (%)	F_f/F_i (%)	F_p/F_i (%)	C_{Df}	C_{Dp}
01	5.88	111.78	31.89	68.11	0.0169	1.4430
02	5.33	101.23	35.65	64.35	0.0171	1.2354
03	6.05	114.86	30.65	69.35	0.0167	1.5102
04	5.59	106.20	34.02	65.98	0.0171	1.3281
05	5.42	102.90	35.37	64.63	0.0173	1.2607
06	5.44	103.30	34.85	65.15	0.0171	1.2760
07	5.70	108.35	32.90	67.10	0.0169	1.3787
08	5.86	111.43	33.69	66.31	0.0178	1.4006
09	4.97	94.38	35.49	64.51	0.0159	1.1540
10	4.68	88.88	36.55	63.45	0.0154	1.0689
11	5.05	96.00	35.12	64.88	0.0160	1.1810
12	6.00	113.98	32.47	67.53	0.0175	1.4589
13	5.10	96.84	34.18	65.82	0.0157	1.2081
14	4.80	91.21	35.90	64.05	0.0155	1.1079
15	4.84	92.00	35.74	64.26	0.0156	1.1209
16	5.30	100.71	33.48	66.52	0.0160	1.2702
17	4.63	88.05	36.30	63.70	0.0151	1.0637
18	4.67	88.71	36.37	63.63	0.0153	1.0701
19	4.69	89.19	36.08	63.92	0.0153	1.0810

The pressure drag coefficient C_{Dp} is usually not considered because of the thin plate assumption; however, the results discussed above have demonstrated that the resistance from the small frontal area cannot be neglected. This is confirmed by the percentage contributions of friction and pressure to the overall drag for each plate that are listed in Table 2. The total drag is calculated by summing up the overall drag for all individual plates; that is, $F_t = \sum_{i=1}^{n_p} F_i$, whereas the averaged drag $F_a = F_t/n_p$ is used to normalize the plate drag. By inspecting the detailed data in Table 2, C_{Df} is found to be in good agreement with the theoretical value of $C_{Df} = 0.0174$ and C_{Dp} is around the experimental data, $C_{Dp} = 1.3$, for a plate with height-to-width ratio of 3.0 (Blevins, 1984). In accordance with the distribution of drag force at the plate scale, drag coefficients of plates in the free group are significantly greater than those of plates in the wake group. Noteworthy is that the variation of the friction drag coefficients within both groups is fairly uniform, with relatively little deviation from the group mean value. In contrast, the pressure drag coefficients of plates on the periphery are greater than those of plates on the centerline within both groups (e.g., $C_{Dp} = 1.4430$ for P_{01} and $C_{Dp} = 1.2354$ for P_{02}). As drag coefficients can be regarded as normalized drag force, the tabulated values reveal a close relationship between the drag acting on a plate and its position in the patch.

In order to better visualize the spatial variation of the drag force at the plate scale, Figure 15 visualizes the ratio of individual plate drag to the patch average, F_i/F_a (left column), the ratio of pressure drag to individual drag of each plate, F_p/F_i (middle column), and the ratio of friction drag to individual drag of each plate, F_f/F_i (right column), for the three cases. The distribution of the drag of individual plates in comparison with the average plate drag (left column) exhibits significant spatial heterogeneity: The plates in the free group are subject to larger drag force than those in the wake group, exemplifying the so-called sheltering effect (Raupach, 1992). The plates on the periphery experience significantly more pressure drag than the ones on the centerline, this is most noteworthy the densest configuration and reflects that flow diversion (spanwise fluxes) at patch scale has a big impact on the hydrodynamics at plate scale. The middle column of Figure 15 visualizes that the ratio of friction drag to the total drag of the plates in the free group is noticeably less than the one of the plates in the wake group. Case 3 is the most extreme in that regard and for the plates of the free group on the periphery only 25% of the total drag on that plate is due to friction, whereas a plate in the wake group nearly 40% of the total drag is due to friction drag. This is consistent with the analysis of boundary layer thicknesses that was presented above, namely, that the shear becomes stronger as the boundary layer thins, producing higher friction drag. The opposite is true when considering the ratio of

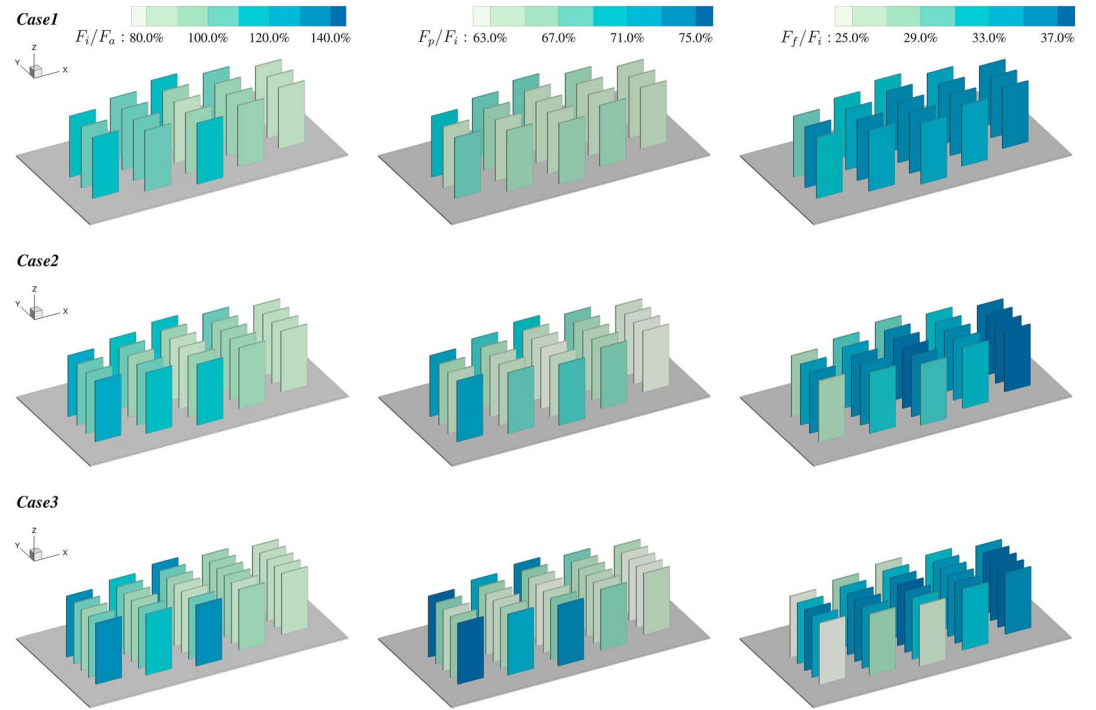


Figure 15. The ratio of individual plate drag force to patch average drag force F_i/F_a (left column), the ratio of pressure drag to individual drag of each plate, F_p/F_i (middle column), and the ratio of friction drag to individual drag of each plate, F_f/F_i (right column), for the three cases.

pressure drag to the total drag of each plate. Here the free group plates, and in particular those that are located at the periphery of the patch, are subjected to the highest amount of pressure drag, whereas those located in the wake of up stream plates experience less pressure drag. Table 2 quantifies the drag characteristics of the individual plates and their relative contributions to the patch-scale drag. Free group plates contribute more to the total drag than wake-group plates, and the relative contribution of friction drag (F_f/F_i) increases from the free group to the wake group for Case 1 (e.g., $F_f/F_i = 31.89\%$ for Plate 01 and 36.37% for Plate 18). At the same time pressure drag reduces from free-group plates (e.g., P_{01} , $F_p/F_i = 68.11\%$) to wake-group plates (e.g., P_{18} , $F_p/F_i = 63.63$). Also noteworthy is that the variation of the friction/drag coefficients within both groups is fairly uniform, with relatively little deviation from the group mean value, although it is noticeable that the plates in the middle of the patch tend to be subjected to higher drag than those located on the periphery of the patch, especially those of the free group, with the exception of the two plates located furthest from the patch centerline (P_{08} and P_{12} for Case 1).

At the patch scale, the bulk drag coefficient C_D is obtained from the total drag force using

$$F_t = \frac{1}{2} C_D u_{\text{bulk}}^2 B H_p. \quad (13)$$

The value of C_D for the three cases is 0.2729, 0.3505, and 0.4214, suggesting a linear correlation with the number of plates (19, 24, and 29). For reference, a solid body with an elliptical planform and minor-axis-to-major-axis ratio of 0.5, subjected to similar flow conditions as herein, has a drag coefficient of approximately 0.6 (Blevins, 1984; note that the minor-axis-to-major-axis ratio of the patches in the present investigation is approximately 0.34), underlining the fact that the effect of decreasing patch density can be quantified by adjusting (decreasing) the drag coefficient. Figure 16 presents the relative contributions of friction and pressure drag to the total drag for the three flow cases. Noteworthy is the fact that the contribution of pressure drag is nearly twice that of friction drag and that this ratio is not very sensitive to the plate density of the patch. The relative contribution of the pressure drag only increases from 65% of the total drag for Case 1 to 67% of the total drag for the densest patch, that is, Case 3. It demonstrates that the drag characteristics of individual plates, see Figure 15, is governed by the hydrodynamics at the patch scale.

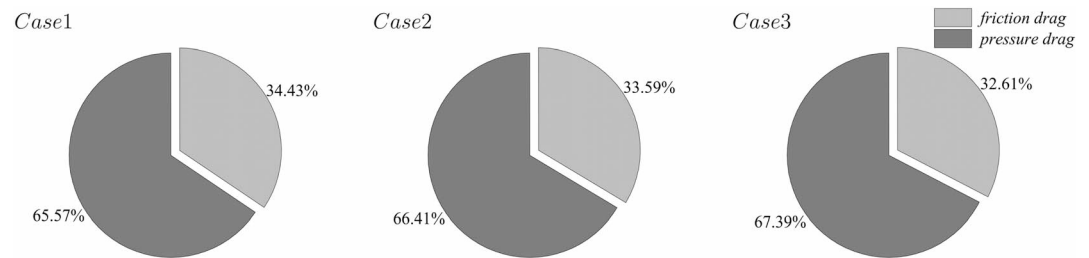


Figure 16. Percentage contributions of friction and pressure drag (patch averages).

6. Conclusions

The results of LES of flow through porous patches composed of an array of thin plates have been presented. The distributions of streamwise velocity and vertical vorticity in the horizontal plane showed the hydrodynamics to be significantly different between plates that face the undisturbed approach flow and plates that are located downstream of other plates. It has been proposed to divide the plates into two groups: the free group and the wake group, based on their position within the patch. The plate boundary layers in the free group are close to laminar and thus may be approximated by an analytical solution (for instance, the Blasius solution) for flow over an isolated flat plate. In contrast, plates that are part of the wake-group feature thicker (turbulent) boundary layers due to turbulent perturbations introduced by trailing edge vortices of upstream plates.

It has been shown that spanwise fluxes occur at the patch-scale and divert the flow toward the sides of the patch which affects boundary layer development on the plates that are located at the periphery of the patch. These plates are characterized by a rather thick boundary layer (thicker than the Blasius solution) while plates that are located inside the patch experience rather Poiseuille-type flow conditions, and hence, their boundary layer growth is restricted by the presence of neighboring (or opposite) plates and these boundary layers show a rather asymptotic behavior. Subsequently, the plate location within the patch also affects the plates' drag characteristics. The plates that are located at the periphery of the patch generally encounter greater pressure drag than plates that are located inside the patch. The plates that experience Poiseuille-type flow have a relatively high friction drag, which is owing to the fact that the near wall streamwise velocity gradients are greater than those of the plates that are located at the periphery. The plates in the wake group benefit from a sheltering effect; that is, the friction drag and the pressure drag are less in comparison with the respective drag of the plates of the free group. It has been found that the pressure drag resulting from the thin frontal area of the plate is nearly double the friction drag acting on the plate's lateral area, even though the length-to-width ratio of the plates is large. The density of the patch does not affect markedly the contribution of pressure (65% of the total drag) and friction (35%) drag to the total drag.

Acknowledgments

This research is funded by the National Key Research and Development Program of China (2018YFC0407606) and the National Natural Science Foundation of China (51379059). Yiqing Gong is funded by the CSC (China Scholarship Council). The data and model used in this paper are available on HydroShare at the <http://www.hydroshare.org/resource/fd7ad0a002e94f468906fcf468405bbb> website.

References

- Albayrak, I., Nikora, V., Miler, O., & O'Hare, M. (2012). Flow-plant interactions at a leaf scale: Effects of leaf shape, serration, roughness and flexural rigidity. *Aquatic Sciences*, *74*(2), 267–286. <https://doi.org/10.1007/s00027-011-0220-9>
- Blevins, R. D. (1984). *Applied fluid dynamics handbook* (pp. 568). New York: Van Nostrand Reinhold Co.
- Bouma, T. J., Friedrichs, M., Van Wesenbeeck, B. K., Temmerman, S., Graf, G., & Herman, P. M. J. (2009). Density-dependent linkage of scale-dependent feedbacks: A flume study on the intertidal macrophyte *Spartina anglica*. *Oikos*, *118*(2), 260–268. <https://doi.org/10.1111/j.1600-0706.2008.16892.x>
- Bouma, T. J., van Duren, L. A., Temmerman, S., Claverie, T., Blanco-Garcia, A., Ysebaert, T., & Herman, P. M. J. (2007). Spatial flow and sedimentation patterns within patches of epibenthic structures: Combining field, flume and modelling experiments. *Continental Shelf Research*, *27*(8), 1020–1045. <https://doi.org/10.1016/j.csr.2005.12.019>
- Cevheri, M., McSherry, R., & Stoesser, T. (2016). A local mesh refinement approach for large-eddy simulations of turbulent flows. *International Journal for Numerical Methods in Fluids*, *82*(5), 261–285. <https://doi.org/10.1002/fld.4217>
- Chen, Z., Ortiz, A., Zong, L., & Nepf, H. (2012). The wake structure behind a porous obstruction and its implications for deposition near a finite patch of emergent vegetation. *Water Resources Research*, *48*, W09517. <https://doi.org/10.1029/2012WR012224>
- Defina, A., & Bixio, A. C. (2005). Mean flow and turbulence in vegetated open channel flow. *Water Resources Research*, *41*, W07006. <https://doi.org/10.1029/2004WR003475>
- Fischer-Antze, T., Stoesser, T., Bates, P., & Olsen, N. R. B. (2001). 3D numerical modelling of open-channel flow with submerged vegetation. *Journal of Hydraulic Research*, *39*(3), 303–310. <https://doi.org/10.1080/00221680109499833>
- Follett, E. M., & Nepf, H. M. (2012). Sediment patterns near a model patch of reedy emergent vegetation. *Geomorphology*, *179*, 141–151. <https://doi.org/10.1016/j.geomorph.2012.08.006>

- Hurd, C. L., Stevens, C. L., Laval, B. E., Lawrence, G. A., & Harrison, P. J. (1997). Visualization of seawater flow around morphologically distinct forms of the giant kelp *Macrocystis integrifolia* from wave-sheltered and exposed sites. *Limnology and Oceanography*, *42*(1), 156–163. <https://doi.org/10.4319/lo.1997.42.1.0156>
- Jarrin, N., Benhamadouche, S., Laurence, D., & Prosser, R. (2006). A synthetic-eddy-method for generating inflow conditions for large-eddy simulations. *International Journal of Heat and Fluid Flow*, *27*(4), 585–593. <https://doi.org/10.1016/j.ijheatfluidflow.2006.02.006>
- Jones, C. G., Lawton, J. H., & Shachak, M. (1994). Organisms as ecosystem engineers. *Oikos*, *69*(3), 373–386. <https://doi.org/10.2307/3545850>
- Kadlec, R. H. (1990). Overland flow in wetlands: Vegetation resistance. *Journal of Hydraulic Engineering*, *116*(5), 691–706. [https://doi.org/10.1061/\(ASCE\)0733-9429\(1990\)116:5\(691\)](https://doi.org/10.1061/(ASCE)0733-9429(1990)116:5(691))
- Kara, M. C., Stoesser, T., & McSherry, R. (2015). Calculation of fluid–structure interaction: Methods, refinements, applications. *Proceedings of the ICE - Engineering and Computational Mechanics*, *168*(2), 59–78. <https://doi.org/10.1680/eacm.15.00010>
- Kara, S., Stoesser, T., Sturm, T. W., & Mulahasan, S. (2015). Flow dynamics through a submerged bridge opening with overtopping. *Journal of Hydraulic Research*, *53*(2), 186–195.
- Kara, S., Stoesser, T., Sturm, T. W., & Mulahasan, S. (2015). Free-surface versus rigid-lid LES computations for bridge-abutment flow. *Journal of Hydraulic Engineering*, *141*(9), 04015,019–1.
- Kim, S. J., & Stoesser, T. (2011). Closure modeling and direct simulation of vegetation drag in flow through emergent vegetation. *Water Resources Research*, *47*, W10511. <https://doi.org/10.1029/2011WR010561>
- Kouwen, N., Unny, T. E., & Hill, H. M. (1969). Flow retardance in vegetated channels. *Journal of the Irrigation and Drainage Division*, *95*(2), 329–344.
- López, F., & García, M. H. (2001). Mean flow and turbulence structure of open-channel flow through non-emergent vegetation. *Journal of Hydraulic Engineering*, *127*(5), 392–402. [https://doi.org/10.1061/\(ASCE\)0733-9429\(2001\)127:5\(392\)](https://doi.org/10.1061/(ASCE)0733-9429(2001)127:5(392))
- Liu, D., Diplas, P., Fairbanks, J. D., & Hodges, C. C. (2008). An experimental study of flow through rigid vegetation. *Journal of Geophysical Research*, *113*, F04015. <https://doi.org/10.1029/2008JF001042>
- Meire, D. W. S. A., Kondziolka, J. M., & Nepf, H. M. (2014). Interaction between neighboring vegetation patches: Impact on flow and deposition. *Water Resources Research*, *50*, 3809–3825. <https://doi.org/10.1002/2013WR015070>
- Miler, O., Albayrak, I., Nikora, V., & O'Hare, M. (2012). Biomechanical properties of aquatic plants and their effects on plant-flow interactions in streams and rivers. *Aquatic Sciences*, *74*(1), 31–44. <https://doi.org/10.1007/s00027-011-0188-5>
- Munson, B. R., Rothmayer, A. P., & Okiishi, T. H. (2012). *Fundamentals of fluid mechanics* (7th ed.). Hoboken, NJ: Wiley.
- Nepf, H. M. (1999). Drag, turbulence, and diffusion in flow through emergent vegetation. *Water Resources Research*, *35*(2), 479–489. <https://doi.org/10.1029/1998WR900069>
- Nepf, H. M. (2011). Treatise on estuarine and coastal science. In *Flow over and through biota*. Amsterdam: Elsevier Inc.
- Nezu, I., & Sanjou, M. (2008). Turbulence structure and coherent motion in vegetated canopy open-channel flows. *Journal of Hydro-Environment Research*, *2*(2), 62–90. <https://doi.org/10.1016/j.jher.2008.05.003>
- Nicoud, F., & Ducros, F. (1999). Subgrid scale stress modelling based on the squared of the velocity gradient tensor. *Flow, Turbulence and Combustion*, *62*(3), 183–200.
- Nikora, V. (2010). Hydrodynamics of aquatic ecosystems: An interface between ecology, biomechanics and environmental fluid mechanics. *River Research and Applications*, *26*(4), 367–384. <https://doi.org/10.1002/rra.1291>
- Okamoto, T.-A., & Nezu, I. (2010). Large eddy simulation of 3-D flow structure and mass transport in open-channel flows with submerged vegetations. *Journal of Hydro-environment Research*, *4*(3), 185–197. <https://doi.org/10.1016/j.jher.2010.04.015>
- Ouro, P., Fraga, B., Lopez-Novoa, U., & Stoesser, T. (2019). Scalability of an Eulerian-Lagrangian large-eddy simulation solver with hybrid MPI/OpenMP parallelisation. *Computers & Fluids*, *179*, 123–136.
- Ouro, P., Harrold, M., Stoesser, T., & Bromley, P. (2017). Hydrodynamic loadings on a horizontal axis tidal turbine prototype. *Journal of Fluids and Structures*, *71*, 78–95. <https://doi.org/10.1016/j.jfluidstructs.2017.03.009>
- Ouro, P., & Stoesser, T. (2017). An immersed boundary-based large-eddy simulation approach to predict the performance of vertical axis tidal turbines. *Computers & Fluids*, *152*, 74–87. <https://doi.org/10.1016/j.compfluid.2017.04.003>
- Ouro, P., & Stoesser, T. (2018). Impact of environmental turbulence on the performance and loadings of a tidal stream turbine. *Flow, Turbulence and Combustion*, *102*, 613–639. <https://doi.org/10.1007/s10494-018-9975-6>
- Poggi, D., Porporato, A., Ridolfi, L., Albertson, J. D., & Katul, G. G. (2004). The effect of vegetation density on canopy sub-layer turbulence. *Boundary-Layer Meteorology*, *111*(3), 565–587. <https://doi.org/10.1023/B:BOUN.0000016576.05621.73>
- Raupach, M. R. (1992). Drag and drag partition on rough surfaces. *Boundary-Layer Meteorology*, *60*(4), 375–395. <https://doi.org/10.1007/BF00155203>
- Roma, A. M., Peskin, C. S., & Berger, M. J. (1999). An adaptive version of the immersed boundary method. *Journal of Computational Physics*, *153*(2), 509–534. <https://doi.org/10.1006/jcph.1999.6293>
- Rominger, J. T., & Nepf, H. M. (2011). Flow adjustment and interior flow associated with a rectangular porous obstruction. *Journal of Fluid Mechanics*, *680*, 636–659. <https://doi.org/10.1017/jfm.2011.199>
- Shu, C.-W. (2009). High order weighted essentially nonoscillatory schemes for convection dominated problems. *SIAM Review*, *51*(1), 82–126. <https://doi.org/10.1137/070679065>
- Siniscalchi, F., Nikora, V. I., & Aberle, J. (2012). Plant patch hydrodynamics in streams: Mean flow, turbulence, and drag forces. *Water Resources Research*, *48*, W01513. <https://doi.org/10.1029/2011WR011050>
- Statzner, B. (2008). How views about flow adaptations of benthic stream invertebrates changed over the last century. *International Review of Hydrobiology*, *93*(4-5), 593–605. <https://doi.org/10.1002/iroh.200711018>
- Stoesser, T. (2014). Large-eddy simulation in hydraulics: Quo vadis? *Journal of Hydraulic Research*, *52*(4), 441–452.
- Stoesser, T., Kim, S. J., & Diplas, P. (2010). Turbulent flow through idealized emergent vegetation. *Journal of Hydraulic Engineering-Asce*, *136*(12), 1003–1017. [https://doi.org/10.1061/\(ASCE\)Hy.1943-7900.0000153](https://doi.org/10.1061/(ASCE)Hy.1943-7900.0000153)
- Stoesser, T., & Nikora, V. (2008). Flow structure over square bars at intermediate submergence: Large eddy simulation study of bar spacing effect. *Acta Geophysica*, *56*(3), 876–893. <https://doi.org/10.2478/s11600-008-0030-1>
- Stoesser, T., Salvador, G. P., Rodi, W., & Diplas, P. (2009). Large eddy simulation of turbulent flow through submerged vegetation. *Transport in Porous Media*, *78*(3 SPEC. ISS.), 347–365. <https://doi.org/10.1007/s11242-009-9371-8>
- Stoesser, T., Wilson, CAME, Bates, P. D., & Dittrich, A. (2003). Application of a 3D numerical model to a river with vegetated floodplains. *Journal of Hydroinformatics*, *5*(2), 99–112.
- Tanino, Y., & Nepf, H. M. (2008). Laboratory investigation of mean drag in a random array of rigid, emergent cylinders. *Journal of Hydraulic Engineering*, *134*(January), 34–41. [https://doi.org/10.1061/\(ASCE\)HY.1943-7900.0000080](https://doi.org/10.1061/(ASCE)HY.1943-7900.0000080)

- Thomas, F. I. M., Cornelisen, C. D., & Zande, J. M. (2000). Effects of water velocity and canopy morphology on ammonium uptake by seagrass communities. *Ecology*, *81*(10), 2704–2713. [https://doi.org/10.1890/0012-9658\(2000\)081\[2704:EOWVAC\]2.0.CO;2](https://doi.org/10.1890/0012-9658(2000)081[2704:EOWVAC]2.0.CO;2)
- Vandenbruwaene, W., Temmerman, S., Bouma, T. J., Klaassen, P. C., De Vries, M. B., Callaghan, D. P., et al. (2011). Flow interaction with dynamic vegetation patches: Implications for biogeomorphic evolution of a tidal landscape. *Journal of Geophysical Research*, *116*, F01008. <https://doi.org/10.1029/2010JF001788>
- Vogel, S. (1994). *Life in moving fluids: The physical biology of flow*. Princeton, NJ: Princeton University Press.
- Wunder, S., Trevisson, M., Hecke, C., Chagot, L., Murphy, B., McLelland, S., et al. (2018). Near wake of emergent vegetation patches in shallow flow. *E3S Web of Conferences, Riverflow 2018*, *40*, 02057. <https://doi.org/10.1051/e3sconf/20184002057>
- Zong, L., & Nepf, H. (2012). Vortex development behind a finite porous obstruction in a channel. *Journal of Fluid Mechanics*, *691*, 368–391. <https://doi.org/10.1017/jfm.2011.479>